PHYSICAL REVIEW E **92**, 023005 (2015)

Origin of nonlinearity and plausible turbulence by hydromagnetic transient growth in accretion disks: Faster growth rate than magnetorotational instability

Sujit Kumar Nath[*] and Banibrata Mukhopadhyay[†]
Department of Physics, Indian Institute of Science, Bangalore 560012, India

(Received 9 October 2014; revised manuscript received 15 June 2015; published 5 August 2015)

We investigate the evolution of hydromagnetic perturbations in a small section of accretion disks. It is known that molecular viscosity is negligible in accretion disks. Hence, it has been argued that a mechanism, known as magnetorotational instability (MRI), is responsible for transporting matter in the presence of a weak magnetic field. However, there are some shortcomings, which question the effectiveness of MRI. Now the question arises, whether other hydromagnetic effects, e.g., transient growth (TG), can play an important role in bringing nonlinearity into the system, even at weak magnetic fields. In addition, it should be determined whether MRI or TG is primarily responsible for revealing nonlinearity in order to make the flow turbulent. Our results prove explicitly that the flows with a high Reynolds number (Re), which is the case for realistic astrophysical accretion disks, exhibit nonlinearity via TG of perturbation modes faster than that by modes producing MRI. For a fixed wave vector, MRI dominates over transient effects only at low Re, lower than the value expected to be in astrophysical accretion disks, and low magnetic fields. This calls into serious question the (overall) persuasiveness of MRI in astrophysical accretion disks.

DOI: 10.1103/PhysRevE.92.023005 PACS number(s): 47.27.T−, 95.30.Qd, 98.62.Mw, 47.35.Tv

I. INTRODUCTION

Accretion disks are found in active galactic nuclei (AGNs), around compact stellar objects in a binary system, around newly formed stars, etc. (see, e.g., [1]). However, the working principle of accretion disks remains enigmatic. Due to its inadequate molecular viscosity, turbulent viscosity has been proposed to explain the transport of matter toward a central object. This idea is particularly attractive because of its high Reynolds number, $\mathrm{Re} \gtrsim 10^{14}$ (see, e.g., [2]). However, the Keplerian disks, which are relevant to many astrophysical applications, are remarkably Rayleigh-stable. Therefore, linear perturbation cannot induce the onset of turbulence, and consequently it cannot provide enough viscosity to transport matter inward therein.

With the application of magnetorotational instability (MRI) [3,4] to Keplerian disks, Balbus and Hawley [5] showed that a weak magnetic field can lead to the exponential growth of the velocity and magnetic-field perturbations. Within a few rotation times, such exponential growth could reveal the onset of turbulence. Since then, MRI has been a widely accepted mechanism to explain the origin of instability and hence the transport of matter in accretion disks. Note that for flows with strong magnetic fields, where the magnetic field is tightly coupled with the flow, MRI is not expected to work. Hence, it is very clear that the MRI is bounded in a small regime of parameter values when the field is weak.

It has been well established by several works that transient growth (TG) can reveal nonlinearity and a transition to turbulence at subcritical Re (e.g., [6–11]). Such a subcritical transition to turbulence was invoked to explain colder purely hydrodynamic accretion flows, e.g., quiescent cataclysmic variables, in protoplanetary and star-forming disks, and in the outer region of disks in active galactic nuclei. Baroclinic instability is another plausible source of vigorous turbulence in colder accretion disks [12]. Note that while hotter flows are expected to be ionized enough to produce weak magnetic fields therein and subsequent MRI, colder flows may remain practically neutral in charge, and hence any instability and turbulence therein must be hydrodynamic. However, in the absence of magnetic effects, the Coriolis force does not allow any significant TG in accretion disks in three dimensions, independent of Re (see [6]), while in purely two dimensions, TG could be large at large Re. However, a pure two-dimensional flow is a very idealistic case. Nevertheless, in the presence of a magnetic field, even in three dimensions, TG could be very large (the Coriolis effect could not suppress the growth). Hence, in a real three-dimensional flow, it is very important to explore magnetic TG.

In the present paper, we explore the relative strengths of MRI and TG in magnetized accretion flows in order to explain the generic origin of nonlinearity and plausible turbulence therein. By TG, we mean the short-time scale growth due to shearing perturbation waves, producing a peak followed by a dip. By MRI, we mean the exponential growth caused by static perturbation waves. While TG may reveal nonlinearity in the system, depending on Re, the amplitude of the initial perturbation and its wave vector, and the background rotational profile of the flow, the question is, can its growth rate be fast enough to compete with that of MRI? On the other hand, is there any limitation of MRI, apart from the fact that MRI does not work at strong magnetic fields? Note that some limitations of MRI were already discussed by previous authors [11,13–16], which then question the origin of viscosity in accretion disk.

We show below that three-dimensional TG dominates over the growth due to MRI modes at large Re, bringing nonlinearity in the flows. This is of immense interest, as the larger Re is more plausible in accretion disks. By comparing modes corresponding to static (original MRI) and shearing (TG) waves, the growth estimates from static MRI waves

---

[*] sujitkumar@physics.iisc.ernet.in

[†] Author to whom all correspondence should be addressed: bm@physics.iisc.ernet.in

have already been argued to be misleading [17]. Throughout their work, previous authors [17] argued that shearing wave structures always grow faster over short time scales than static structures, which we also plan to elaborate on here. Nevertheless, those authors [17] did not explore the length of time over which the short-time growth can persist, which is very important for revealing nonlinearity, which we plan to explicitly explore here. We will show below that in a shorter time scale, TG reveals nonlinearity in the system.

We explicitly calculate the magnetic-field strength above which MRI does not work. Moreover, for a fixed perturbation (which might not correspond to either the best MRI or the best TG mode) with finite Re, we show that with an increase of Re the TG tends to bring the nonlinearity in the systems before MRI could do the same, producing a large growth of perturbation. We notice that above a threshold Re, only TG is sufficient to make the system nonlinear at low magnetic field, and there is no growth at high magnetic fields. Hence, in the regimes of high magnetic field or/and high Re, MRI is not important at all. The working regime of MRI is actually much narrower than is generally believed. As TG was argued to be a plausible source of nonlinearity in cold disks, and the growth due to MRI is subdominant compared to TG at high Re in hot disks, TG could be argued to be the source of nonlinearity and plausible turbulence and subsequent viscosity in any accretion disk.

In the next section, we discuss the perturbation equations describing flows. Subsequently, we explore the total-energy growth of perturbations due to TG and MRI for different parameter values, and we compare the respective parameter spaces for different initial amplitudes of perturbations in Secs. III and IV, respectively. Finally, we end with a discussion in Sec. V.

II. GOVERNING EQUATIONS DESCRIBING MAGNETIZED ROTATING SHEAR FLOWS IN LAGRANGIAN COORDINATES

Within a local shearing box in Lagrangian coordinates, the Navier-Stokes, continuity, and magnetic induction equations and the solenoidal condition (for magnetic field) can be written as

$$\dot{\mathbf{v}} = -\frac{1}{\rho}c_s^2\nabla\rho + \nu\nabla^2\mathbf{v} + 2\mathbf{v}\times\mathbf{\Omega} + \frac{1}{4\pi\rho}\mathbf{B}\cdot\nabla\mathbf{B}, \tag{1}$$

$$\frac{d\rho}{dt} = -\rho\nabla\cdot\mathbf{v}, \tag{2}$$

$$\frac{\partial\mathbf{B}}{\partial t} = \nabla\times(\mathbf{v}\times\mathbf{B}),\ \nabla\cdot\mathbf{B} = \mathbf{0}, \tag{3}$$

when

$$\dot{\mathbf{r}} = \mathbf{v}(\mathbf{r}^L),\ \nabla \equiv \frac{\partial\mathbf{r}^\mathbf{L}}{\partial\mathbf{r}}\cdot\nabla^\mathbf{L}, \tag{4}$$

where $\mathbf{v}$ is the velocity vector, $\mathbf{B}$ is the magnetic field, ν is the kinematic coefficient of viscosity, c_s is the sound speed in the shearing box, $\mathbf{\Omega}$ is the angular velocity, ρ is the density, and $\mathbf{r}$ and $\mathbf{r}^L$ are the position vectors in Eulerian and Lagrangian coordinates, respectively [7]. Note that the contribution of magnetic pressure has been included in the total pressure in the first term on the right-hand side of Eq. (1). For incompressible flow, Eq. (2) becomes

$$\nabla\cdot\mathbf{v} = \mathbf{0}. \tag{5}$$

Let us define the tensor $\Omega\mathsf{q}$, which is the minus of the gradient of the unperturbed (background) velocity field $\mathbf{v}_0 = (0, -q\Omega x, 0)$, as

$$\Omega\mathsf{q} \equiv -\nabla\mathbf{v}_0 = -(\nabla\mathbf{\Omega})\times\mathbf{R} = \begin{pmatrix} 0 & q\Omega & 0 \\ 0 & 0 & 0 \\ 0 & 0 & 0 \end{pmatrix},$$

$$q = -\frac{d\ln\Omega}{d\ln R}, \tag{6}$$

where $\mathbf{R} = (R,0,0)$, R is the distance of the comoving shearing box from the center of the disk, and $|\mathbf{\Omega}| = \Omega \propto R^{-q}$ (see [7] for details). Now integrating Eq. (4), we obtain

$$\mathbf{r}^L = \mathbf{r} + \Omega t\mathbf{r}\cdot\mathsf{q} \Rightarrow \frac{\partial\mathbf{r}^\mathbf{L}}{\partial\mathbf{r}} = \mathbf{1} + \Omega t\mathsf{q}, \tag{7}$$

and this gives rise to the relation

$$\nabla \equiv (\mathbf{1} + \Omega t\mathsf{q})\cdot\nabla^L. \tag{8}$$

Since the unperturbed velocity $\mathbf{v}_0$ has a spatial dependence, it has a nonvanishing time derivative in a perturbed Lagrangian coordinate. Therefore, we obtain

$$\dot{\delta\mathbf{v}} = \dot{\mathbf{v}} - \dot{\mathbf{v}}_0 = \dot{\mathbf{v}} - \mathbf{v}\cdot\nabla\mathbf{v}_0 = \dot{\mathbf{v}} + \Omega\mathbf{v}\cdot\mathsf{q}. \tag{9}$$

Perturbing and linearizing Eqs. (1), (2), and (3) and using Eq. (9), we obtain the perturbed Navier-Stokes, continuity, and induction equations and the solenoidal equation for a magnetic field in Lagrangian coordinates as

$$\dot{\delta\mathbf{v}} = -\frac{1}{\rho}c_s^2\nabla\delta\rho + \nu\nabla^2\delta\mathbf{v} + 2\delta\mathbf{v}\times\mathbf{\Omega} + \frac{1}{4\pi\rho}\mathbf{B}\cdot\nabla\delta\mathbf{B} + \Omega\delta\mathbf{v}\cdot\mathsf{q}, \tag{10}$$

$$\dot{\delta\rho} = -\rho\nabla\cdot\delta\mathbf{v}, \tag{11}$$

$$\dot{\delta\mathbf{B}} = \nabla\times(\mathbf{v}\times\delta\mathbf{B} + \delta\mathbf{v}\times\mathbf{B}) + (\mathbf{v}\cdot\nabla)\delta\mathbf{B},\quad \nabla\cdot\delta\mathbf{B} = \mathbf{0}, \tag{12}$$

where $\delta\mathbf{v}$, $\delta\mathbf{B}$, and $\delta\rho$ are the velocity, magnetic-field vectors, and density of perturbation, respectively.

We now work with the incompressible approximation, i.e., $\delta\rho \to 0$ and $c_s^2 \to \infty$, assuming $c_s^2\delta\rho$ to be finite and decomposing the general linear perturbations into a plane-wave form as

$$\delta\mathbf{v},\delta\mathbf{B} \propto \exp(i\mathbf{k}^L\cdot\mathbf{r}^L), \tag{13}$$

when

$$\mathbf{k} = (k_x,k_y,k_z) = (\mathbf{1} + \Omega t\mathsf{q})\cdot\mathbf{k}^L = \left(k_x^L + q\Omega t k_y^L, k_y^L, k_z^L\right), \tag{14}$$

where $\mathbf{k}$ and $\mathbf{k}^L$ are the wave vectors in the Eulerian and Lagrangian coordinates, respectively. Now using a solenoidal condition for the magnetic field, the incompressibility condition, and the plane-wave solution (13), and if we write

Eqs. (10) and (12) (i.e., Navier-Stokes and magnetic induction equations) componentwise, we obtain

$$\delta\dot{v}_x = -i\frac{1}{\rho}c_s^2\delta\rho\left(k_x^L + q\Omega t k_y^L\right) - \nu k^2\delta v_x + 2\Omega\delta v_y + \frac{1}{4\pi\rho}i\delta B_x(B_1k_x + B_2k_y + B_3k_z), \tag{15}$$

$$\delta\dot{v}_y = -i\frac{1}{\rho}c_s^2\delta\rho k_y^L - \nu k^2\delta v_y - 2\Omega\delta v_x + \Omega q\delta v_x + \frac{1}{4\pi\rho}i\delta B_y(B_1k_x + B_2k_y + B_3k_z), \tag{16}$$

$$\delta\dot{v}_z = -i\frac{1}{\rho}c_s^2\delta\rho k_z^L - \nu k^2\delta v_z + \frac{1}{4\pi\rho}i\delta B_z(B_1k_x + B_2k_y + B_3k_z), \tag{17}$$

$$\delta\dot{B}_x = i\delta v_x(B_1k_x + B_2k_y + B_3k_z), \tag{18}$$

$$\delta\dot{B}_y = i\delta v_y(B_1k_x + B_2k_y + B_3k_z) - q\Omega\delta B_x, \tag{19}$$

$$\delta\dot{B}_z = i\delta v_z(B_1k_x + B_2k_y + B_3k_z). \tag{20}$$

For convenience of the solutions, we further define

$$\triangle = k_x\delta v_x + k_y\delta v_y, \quad \zeta = k_x\delta v_y - k_y\delta v_x,$$
$$\triangle_B = k_x\delta B_x + k_y\delta B_y, \quad \zeta_B = k_x\delta B_y - k_y\delta B_x,$$

and for the plane-wave solutions given by Eq. (13), Eqs. (15)–(20) can be recast into

$$\begin{pmatrix}\dot{\triangle}\\ \dot{\zeta}\\ \dot{\triangle}_B\\ \dot{\zeta}_B\end{pmatrix} = \begin{pmatrix}M_{11} & M_{12} & M_{13} & M_{14}\\ M_{21} & M_{22} & M_{23} & M_{24}\\ M_{31} & M_{32} & M_{33} & M_{34}\\ M_{41} & M_{42} & M_{43} & M_{44}\end{pmatrix}\begin{pmatrix}\triangle\\ \zeta\\ \triangle_B\\ \zeta_B\end{pmatrix}, \tag{21}$$

where

$$M_{11} = \frac{-\nu k^4\left(k_x^2 + k_y^2\right) + 2q\Omega k_x k_y k_z^2}{k^2\left(k_x^2 + k_y^2\right)},$$

$$M_{12} = \frac{2\Omega k_z^2\left\{k_x^2 + (1-q)k_y^2\right\}}{k^2\left(k_x^2 + k_y^2\right)},$$

$$M_{13} = \frac{i(B_1k_x + B_2k_y + B_3k_z)}{4\pi\rho}, \quad M_{14} = 0,$$

$$M_{21} = \Omega(q-2), \quad M_{22} = -\nu k^2, \quad M_{23} = 0,$$

$$M_{24} = \frac{i(B_1k_x + B_2k_y + B_3k_z)}{4\pi\rho},$$

$$M_{31} = i(B_1k_x + B_2k_y + B_3k_z),$$

$$M_{32} = 0, \quad M_{33} = 0, \quad M_{34} = 0,$$

$$M_{41} = 0, \quad M_{42} = i(B_1k_x + B_2k_y + B_3k_z),$$

$$M_{43} = \frac{q\Omega\left(k_y^2 - k_x^2\right)}{k_x^2 + k_y^2},$$

$$M_{44} = \frac{2q\Omega k_x k_y}{k_x^2 + k_y^2}.$$

The assumption of incompressibility is justified as follows. If the wavelength of the velocity perturbations is much shorter than the sound horizon for the time of interest (which in the present context is the infall time of matter), then the density perturbations (which are basically the sound waves) reach equilibrium early on, which renders effectively a uniform density during the time scale of interest. For an astrophysical accretion disk around a black hole, which is either geometrically thin or can be approximated as a vertically averaged flow, the half-thickness of the disk is comparable to the sound horizon corresponding to one disk rotation time. Therefore, as described in previous work (e.g., [7]), for processes taking longer than one rotation time, wavelengths shorter than the disk thickness can be approximately treated as incompressible.

Solving the set of differential equations (21), we can calculate $\delta\mathbf{v}$, $\delta\mathbf{B}$, and the energy $\mathcal{E}$ of the perturbation given by

$$\mathcal{E} \propto \left(\delta\mathbf{v}^2 + \frac{\delta\mathbf{B}^2}{4\pi\rho}\right) = \left(\frac{4\pi\rho(\Delta^2 + \zeta^2) + \Delta_B^2 + \zeta_B^2}{(k_x + k_y q t\Omega)^2 + k_y^2} + \frac{4\pi\Delta^2\rho + \Delta_B^2}{k_z^2}\right)\Big/ 8\pi\rho \tag{22}$$

in terms of new variables. To solve the set of Eqs. (21), we have to supply $\delta\mathbf{B}$ and $\delta\mathbf{v}$ at $t = 0$, i.e., the initial perturbation amplitude (IPA). The structure (and evolution) of perturbations is similar to (the same as) that found earlier [6,7,17]. A sample is shown in Fig. 1, demonstrating how an initial leading wave, with a highly stretched structure, evolves to a spherical wave at the maximum of TG and furthermore evolves to a trailing wave during the declining phase of TG. During this evolution of perturbation, observing the associated total energy growth of perturbation, we will now attempt to understand whether the perturbation will sustain or not to give rise to nonlinearity and plausible turbulence and essentially viscosity to help the infall of matter in an accretion disk. With a detailed investigation, we can also understand the relative weight between TG and growth due to MRI (if it is working) in the time of interest. Moreover, we plan to pinpoint the limit of magnetic-field strength above which the MRI is suppressed (indeed MRI works only for weak magnetic fields).

III. TOTAL-ENERGY GROWTH OF PERTURBATIONS FOR DIFFERENT PARAMETER VALUES

The best possible mode for MRI giving rise to the nonlinearity in the system corresponds to the condition $k_z v_{Az}/\Omega = 1$ (when $v_{Az}^2 = B_z^2/4\pi\rho$) [5]. The growth rate for this fastest exponentially growing mode is $3\Omega/4 = 3/4q$ (since in dimensionless units $\Omega = 1/q$) [5,6,18]. Is there any mode for which TG brings in the nonlinearity into the flow (the best possible mode for TG) at a time scale shorter than the rotational time at which the best possible MRI mode brings in the nonlinearity? Note that an approximate emergence of nonlinearity is defined through the measurement

$$\text{Linearity} = \left(\frac{|\delta\mathbf{v}|}{|\mathbf{v}|} + \frac{|\delta\mathbf{B}|}{|\mathbf{B}|}\right). \tag{23}$$

When the linearity is 1, the system will start becoming nonlinear, which will plausibly lead to turbulence. For a Keplerian disk ($q = 3/2$), the best MRI mode brings in the nonlinearity at time scales $\sim$14 and 23, respectively, for IPAs $= 10^{-3}$ and 10^{-5} [when $\log(1/\text{IPA}) = 3t/4q$]. Figure 2

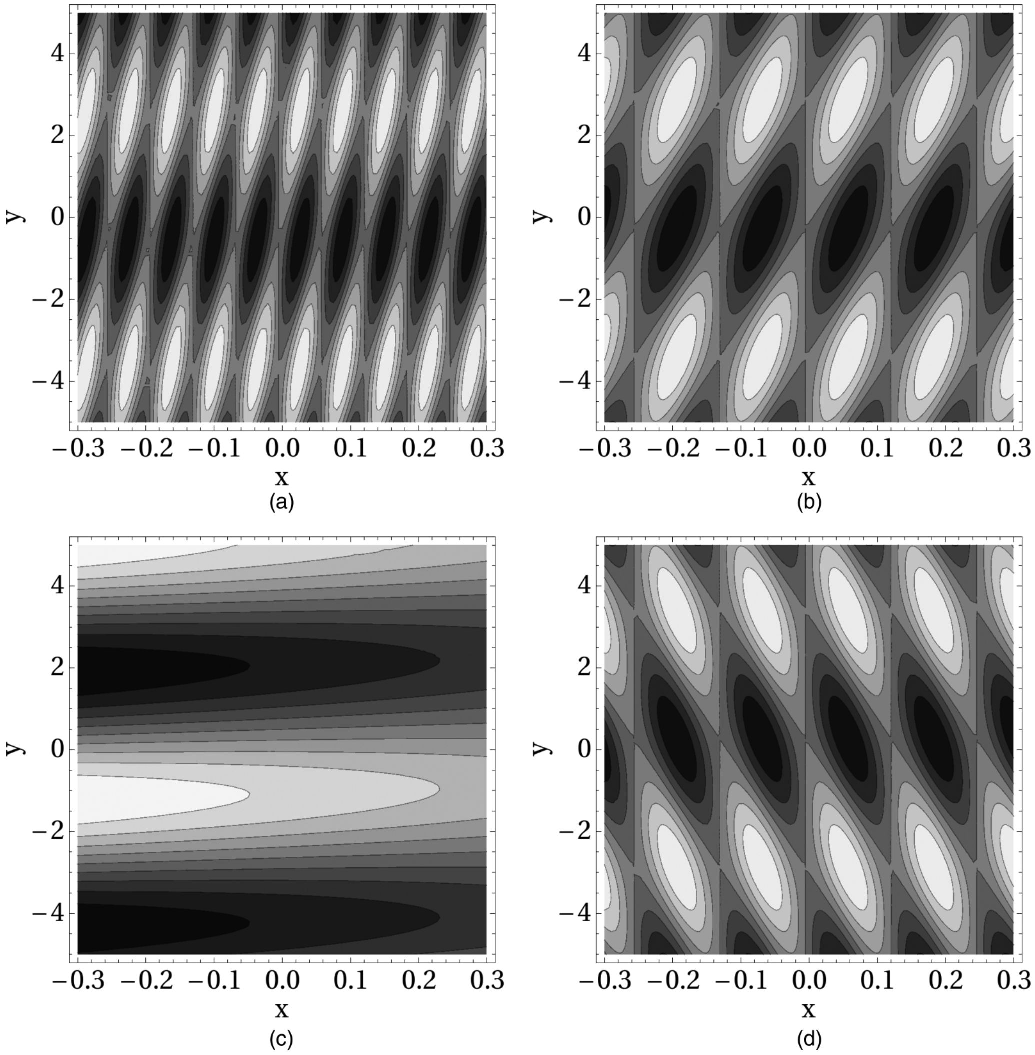

(a)

(b)

(c)

(d)

FIG. 1. Development of the perturbed velocity $\delta v_x(x,y)$ as a function of time, when $\mathrm{Re} = 10^6$, $k_y = 1$, $z = 0$, and $t_{\max}$ denotes the time at which growth attains its maximum, at (a) $t = 0$, (b) $t_{\max}/2$, (c) $t_{\max}$, and (d) $3t_{\max}/2$. The gradual conversion of contour colors from white to black corresponds to the gradual conversion from positive to negative values of $\delta v_x(x,y)$, respectively.

shows that indeed there are modes that reveal nonlinearity via TG at around 3 and 13 rotational times for IPAs 10^{-3} and 10^{-5}, respectively [where $|\delta\mathbf{v}(0)|/|\mathbf{v}|, |\delta\mathbf{B}(0)|/|\mathbf{B}| = \mathrm{IPA}$]. Note from [6] that the maximum TG in two dimensions scales as $\mathrm{TG}_{\max} \sim \mathrm{Re}^{2/3}$ and the corresponding time as $\mathrm{Re}^{1/3}$ in pure hydrodynamical disks. This further corresponds to $k_x^L \sim -\mathrm{Re}^{1/3}$ [19], which reveals that $\mathrm{TG}_{\max}$ corresponds to the minimum of k_x, $k_{x,\min}$ [6,7]. In the same spirit, k_x^L's in Fig. 2 are chosen to be $-\mathrm{Re}^{1/3}$ when initial perturbations are highly stretched and nonspherical. Note that although such a stretched initial wave vector of perturbation is a special choice that is important for the present purposes, nothing prevents them from arising in nature. Since every perturbation mode is equally probable when a system is perturbed (which is indeed the idea behind the choice of the best MRI mode), we explore the mode that is growing faster and leading the system to nonlinearity. In Fig. 3, we relax this Re dependence of k_x^L, but we still obtain the nonlinearity arising at ∼3.5 and ∼6 rotational times for IPAs 10^{-3} and 10^{-5}, respectively. Hence, the full-scale general hydromagnetic effects giving rise to TG reveal nonlinearity in the system faster than that the MRI does, when MRI itself is uncertain. Once the best TG reveals nonlinearity before the best MRI would, the importance of MRI is sluggish in the linear theory. Note that our current emphasis, in particular, is the emergence of nonlinearity via either TG or MRI. However, nonlinearity does not guarantee the transition to turbulence in the physical time scale of accretion. One could argue that MRI modes grow forever, and hence the system would have been turbulent at some point, even if the best MRI modes are not considered when TG would eventually decay. But the important fact to notice here is that as soon as the system becomes nonlinear, MRI (and also TG, if that prevails over MRI) is no longer applicable, as the underlying solution itself is based on linear theory. On the other hand, the effects due to the best possible MRI mode should be compared with that of the best possible TG. Such a comparison shows that TG is more powerful and is actually responsible for bringing nonlinearity into the systems.

Let us move on to the detailed behaviors of TG. In Fig. 4, we show energy growths $[\mathcal{E}(t)/\mathcal{E}(0)]$ for four sets of Re and B^2/ρ (plotted in dimensionless units, based on the dimensions of various quantities of shearing box). We see that for a

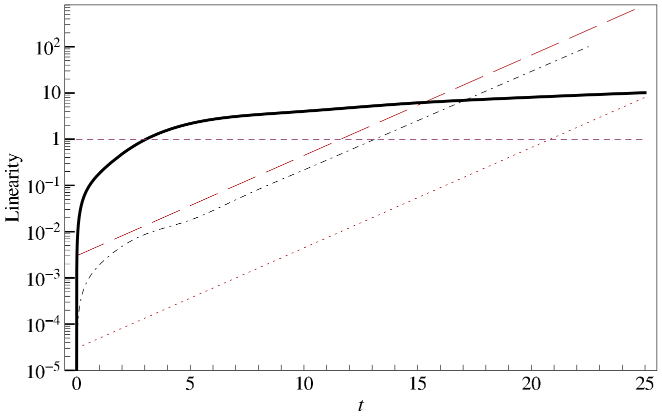

FIG. 2. (Color online) Nonlinearity via best possible TG and MRI. Thick black line corresponds to the TG for IPA $= 10^{-3}$, $\mathrm{Re} = 10^{14}$, $k_x^L = -\mathrm{Re}^{1/3}$, $k_y = 1$, and $k_z = 90K_x^L$; the dot-dashed black line corresponds to the TG for IPA $= 10^{-5}$, $\mathrm{Re} = 10^{25}$, $k_x^L = -\mathrm{Re}^{1/3}$, $k_y = 1$, and $k_z = 90k_x^L$; red long-dashed and dotted lines correspond to the best possible MRI starting from IPA $= 10^{-3}$ and 10^{-5}, respectively. The dashed horizontal line indicates linearity unity.

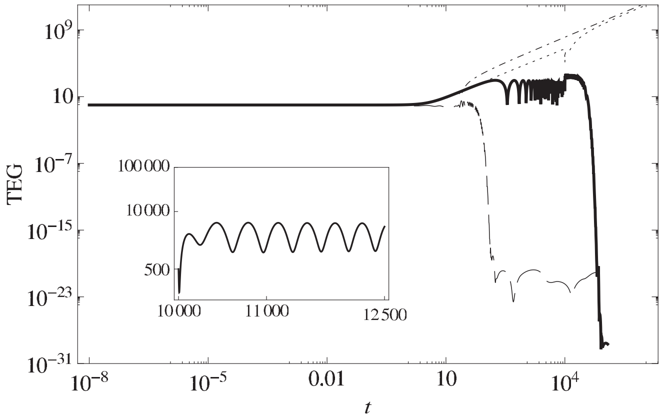

FIG. 4. Total energy growth for different sets of Re and $\mathbf{B} = (0,0,B_3)$: Thick, long-dashed, dotted, and dot-dashed lines correspond, respectively, to $\mathrm{Re} = 10^{12}$ and $B^2/\rho = 10^{-3}$, $\mathrm{Re} = 10^4$ and $B^2/\rho = 10$, $\mathrm{Re} = 10^{12}$ and $B^2/\rho = 10^{-20}$, and $\mathrm{Re} = 10^4$ and $B^2/\rho = 10^{-20}$. $k_x^L = -\mathrm{Re}^{1/3}$, $k_y = k_z = 1$. The inset confirms that the oscillatory zone of the thick line is continuous and smooth.

fixed Re, energy growth of perturbation decays over time if the background magnetic field is large (thick and longdashed lines compared to dotted and dot-dashed lines, respectively). Figure 5 shows the linearity of the respective cases based on Eq. (23). The most important point to be noted from Fig. 5 is that the case of high Re and low **B** (dotted line) exhibits nonlinearity via TG itself for IPA $\approx 10^{-3}$. Note the clear appearance of a TG peak in the linearity as well as growth curves at time $t \sim 10^4$. Later, at the trailing phase of TG, growth starts to increase further due to MRI. However, by this time the system would already become nonlinear, and hence computations of energy growth and growth due to MRI based on the linear theory lose their meaning. However, for a lower Re for the same **B**, growth due to MRI overpowers TG and nonlinearity arises via MRI-induced growth (dot-dashed line).

To understand the global picture and the relative powers of TG and MRI, we perform several numerical experiments, and in Fig. 6 we divide the entire parameter space into three regions, namely MRI-active, TG-active, and stable (or linear) zones for a given perturbation wave vector. Note that for a given **B**, the difference of log(Re) between two successive computations is chosen to be unity, and hence the curve dividing the linearly stable (no energy growth of perturbations) and unstable zones does not appear very smooth. The region to the left of the solid vertical line exhibits nonlinearity via MRI, while that on the right side corresponds to nonlinearity via TG before MRI could kick in.

Hence, a very important message here is that the energy growth rate due to MRI is faster than TG only at lower values of Re, and it is further suppressed above a certain higher **B** (when indeed MRI is a weak field effect). At larger Re, which actually corresponds to astrophysical accretion disks, the growth rate due to TG overpowers that due to MRI. Although Fig. 6 represents cases corresponding to a vertical background magnetic field, we obtain similar trends of results at other

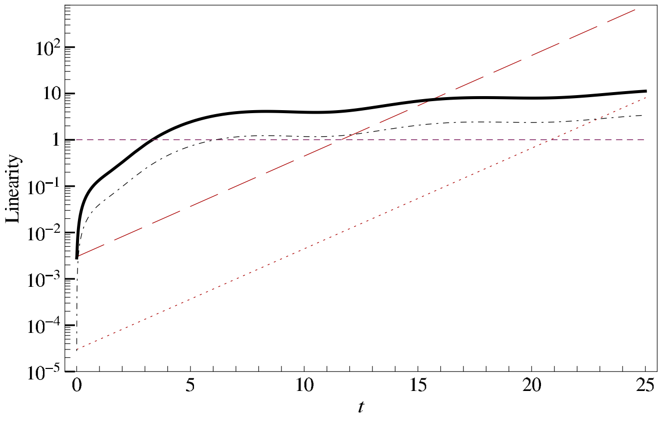

FIG. 3. (Color online) Same as Fig. 2, but the black thick and dot-dashed lines correspond to the TG for $k_x^L = 1$, $k_y = 1$, $k_z = 100$, $\mathrm{Re} = 10^{12}$ and $k_x^L = 1$, $k_y = 1$, $k_z = 3000$, $\mathrm{Re} = 10^{12}$, respectively.

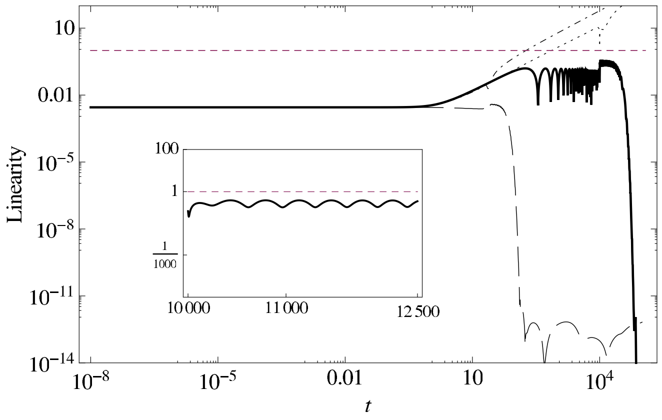

FIG. 5. (Color online) Linearity of the cases in Fig. 4. The dashed horizontal line indicates linearity unity. The inset confirms that the oscillatory zone of the thick line is continuous and smooth.

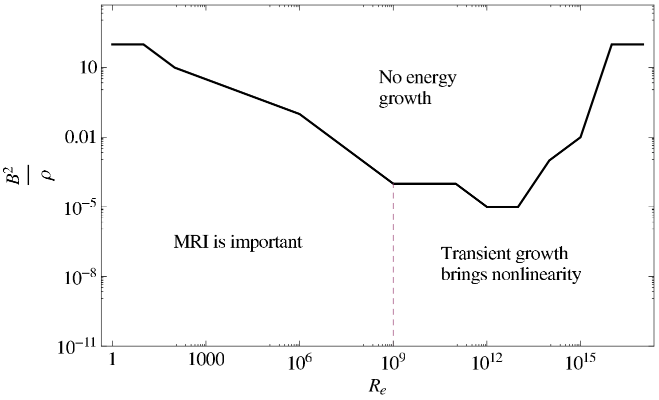

FIG. 6. (Color online) Parameter space describing stable and unstable zones, based on the MRI and TG inactive and active regions, when $\mathbf{B} = (0,0,B_3)$ and IPA is 10^{-3}. The dashed vertical line at $\mathrm{Re} = 10^9$ is the threshold Re above which MRI does not work. $k_x^L = -\mathrm{Re}^{1/3}$, $k_y = k_z = 1$.

background magnetic-field geometries and wave vectors, and hence they are not shown here.

IV. COMPARISON OF PARAMETER SPACE FOR DIFFERENT INITIAL AMPLITUDE OF PERTURBATIONS

Figure 7 compares the parameter spaces, as described in Fig. 6, for two different IPAs: 10^{-3} and 10^{-5}. As IPA decreases, the value of Re dividing the MRI-active and TG-active zones, namely Re_d, increases, which apparently implies that the MRI-active region increases. It also appears that $\mathrm{Re}_d \sim \mathrm{IPA}^{-3}$. Let us now recall the time scale leading to the system being nonlinear by the respective growths due to MRI and TG, and let us estimate if those agree with the observation and the initial choice of our model. For this purpose, first we fix Re at 10^{12} and take the IPA to be 10^{-3}, along with sufficiently low **B**, so that the flow is assured to be nonlinear and unstable in the parameter space described in Figs. 6 and 7. In this case, nonlinearity arises in the TG-active zone at about 750 rotation time, and the corresponding TG is shown in Fig. 5 (dotted line). If the shearing box is at $100R_g$ away from a $10M_\odot$ black hole, where R_g and $M_\odot$ are the Schwarzschild radius and the solar mass, respectively, then this dimensionless time scale recasts into $750L/(q\Omega L) = 750\sqrt{R^3/GMq^2} \sim 750$ s for $q = 1.5$ (Keplerian disk) when L is the radial width of the shearing box, G is Newton's gravitation constant, and M is the mass of the black hole. Now if we decrease IPA to 10^{-5} keeping Re fixed, TG cannot bring nonlinearity anymore (however, by increasing Re, TG could again bring nonlinearity), as shown in Fig. 7. Instead, the nonlinearity arises via MRI modes. However, the time scale for the emergence of nonlinearity in this MRI-active process, as shown in Fig. 5, is approximately 35 000 rotation time, which is ~35 000 s (following the same procedure as used above for the TG-active case to convert the dimensionless to dimensionful times). Now we can calculate the radial velocity (v_r) of the Keplerian accretion disk at the location of the shearing box for a given accretion rate $\dot{M}$, say a 0.1 Eddington rate [20], which is supported by observation, given by [20]

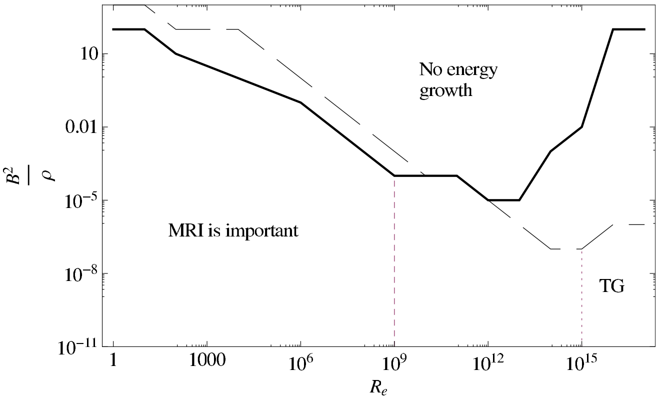

FIG. 7. (Color online) Same as Fig. 6 but comparing results with different IPA, when solid and long-dashed lines are for IPA $= 10^{-3}$ and 10^{-5}, respectively. The dashed and dotted vertical lines at $\mathrm{Re} = 10^9$ and 10^{15} correspond to threshold Re (as in Fig. 6) when IPA $= 10^{-3}$ and 10^{-5}, respectively.

$$v_r = 2\times 10^6 \alpha^{4/5}\left(\frac{\dot{M}}{3\times 10^{-8}M_\odot/\mathrm{year}}\right)^{2/5}\left(\frac{M}{M_\odot}\right)^{-1/5} \times\left(\frac{R}{3R_g}\right)^{-2/5}\left[1-\left(\frac{R}{3R_g}\right)^{-1/2}\right]^{-3/5}, \tag{24}$$

when α is the Shakura-Sunyaev viscosity parameter (whose origin we are actually attempting to determine herein). It is reasonable to assume that the time required to make the flow nonlinear and hence turbulent, which subsequently reveals viscosity, is of the same order as the time required by a fluid parcel to cross the length of the shearing box radially (t_L) as a result of turbulent viscosity. Hence, the product of v_r and t_L should be of the order of the width of the shearing box L. For the above-mentioned case of IPA $= 10^{-3}$, when nonlinearity is due to TG, we obtain $L = 0.1R_g$ from Eq. (24), which is highly reasonable for our choice of a shearing box approximation ($L \ll R$). However, for the case of IPA $= 10^{-5}$, when nonlinearity is due to MRI, we obtain $L = 10R_g$, which marginally satisfies (or even violates) the initial choice of a narrow shearing box at $100R_g$. Therefore, although smaller IPAs increase MRI-active zones, the observed infall cannot be explained by them. This problem with MRI would appear to be more severe at progressively lower IPAs, and TG would be more important for revealing nonlinearity at progressively higher Re, which are forbidden for MRI.

V. DISCUSSION AND CONCLUSIONS

Let us estimate the maximum $|\mathbf{B}|$ in units of G supporting nonlinearity, as shown by the solid curve(s) in Figs. 6 and 7. We again set the shearing box at $100R_g$ away from a $10M_\odot$ black hole. Then we obtain the values of density (ρ_{100R_g}) at that location to be $\sim 10^{-4}$ gm/cm^3 [20]. The background Keplerian velocity at that position for the size of the shearing box, $0.1R_g$, which is consistent with that obtained for the TG active zone, can be obtained as $q\Omega L = q\sqrt{GM/R^3}L \sim 10^6$

cm/s. We now consider $\mathrm{Re} = 10^{12}$, and, hence, from Fig. 6 the corresponding maximum (dimensionless) magnetic field supporting nonlinearity is given by $B^2/\rho = 10^{-5}$. Therefore, the corresponding actual value of the magnetic field is $\sqrt{10^{-5}\rho_{100R_g}(q\Omega L)^2} \sim 30$ G. This means that for the flow with $\mathrm{Re} = 10^{12}$ and $|\mathbf{B}| > 30$ G, the energy growth of perturbation will decay over time, but for $|\mathbf{B}| \leqslant 30$ G, TG will be sufficient to bring nonlinearity in the system, however still not requiring any growth due to MRI. From Fig. 6, it is clear that MRI is only important whenever $\mathrm{Re} < 10^9$, whereas for $\mathrm{Re} \geqslant 10^9$, which is the favorable zone of Re for accretion disks, magnetic TG is more important than MRI.

In short, we have calculated the magnetic-field strengths for different Re's above which the system will be stable under linear perturbation and an upper bound of Re above which either the system is stable under linear perturbation (for high-magnetic-field strength) or reaches nonlinear regime (for low magnetic field) through magnetic TG. In summary, MRI is not the sole mechanism to make accretion disks unstable, there is a large area in which TG rules, and the explanation of accretion solely via MRI is misleading.

ACKNOWLEDGMENTS

The authors would like to thank Prateek Sharma for illuminating discussion. B.M. acknowledges partial support through the research grant provided by Indian Space Research Organization of Ref. No. ISRO/RES/2/367/10-11.

[1] J. E. Pringle, Annu. Rev. Astron. Astrophys. **19**, 137 (1981).
[2] B. Mukhopadhyay, Phys. Lett. B **721**, 151 (2013).
[3] E. Velikhov, J. Exp. Theor. Phys. **36**, 1398 (1959).
[4] S. Chandrasekhar, Proc. Natl. Acad. Sci. (USA) **46**, 253 (1960).
[5] S. A. Balbus and J. F. Hawley, Astrophys. J. **376**, 214 (1991).
[6] B. Mukhopadhyay, N. Afshordi, and R. Narayan, Astrophys. J. **629**, 383 (2005).
[7] N. Afshordi, B. Mukhopadhyay, and R. Narayan, Astrophys. J. **629**, 373 (2005).
[8] G. D. Chagelishvili, J.-P. Zahn, A. G. Tevzadze, and J. G. Lominadze, Astron. Astrophys. **402**, 401 (2003).
[9] P. A. Yecko, Astron. Astrophys. **425**, 385 (2004).
[10] O. M. Umurhan and O. Regev, Astron. Astrophys. **427**, 855 (2004).
[11] M. Avila, Phys. Rev. Lett. **108**, 124501 (2012).
[12] H. H. Klahr and P. Bodenheimer, Astrophys. J. **582**, 869 (2003).
[13] S. M. Mahajan and V. Krishan, Astrophys. J. **682**, 602 (2008).
[14] O. M. Umurhan, K. Menou, and O. Regev, Phys. Rev. Lett. **98**, 034501 (2007).
[15] E. Liverts, Y. Shtemler, M. Mond, O. M. Umurhan, and D. V. Bisikalo, Phys. Rev. Lett. **109**, 224501 (2012).
[16] M. E. Pessah and C. Chan, Astrophys. J. **751**, 48 (2012).
[17] J. Squire and A. Bhattacharjee, Phys. Rev. Lett. **113**, 025006 (2014).
[18] S. A. Balbus and J. F. Hawley, Rev. Mod. Phys. **70**, 1 (1998).
[19] B. Mukhopadhyay, Astrophys. J. **653**, 503 (2006).
[20] N. I. Shakura and R. A. Sunyaev, Astron. Astrophys. **24**, 337 (1973).